NJC

ROYAL SOCIETY OF CHEMISTRY

PAPER

View Article Online
View Journal

Cite this: DOI: 10.1039/d5nj03812j

Thermal and barrier properties of poly(3-hydroxybutyrate) hybrid nanocomposites: use of experimental data for reliable prediction *via* machine learning

Ana M. Díez-Pascual *[a] and José A. Luceño-Sánchez [b]

Poly(3-hydroxybutyrate) (P3HB) is a fully biodegradable polyester used for applications such as drug delivery, tissue engineering and food packaging. However, it presents some drawbacks including brittleness, narrow processing window, high water vapour permeability and low thermal stability. The addition of different nanofillers can improve its performance. In this research, P3HB/sepiolite (SEP)/carbon nanotube (CNT)/tungsten disulfide (WS_2) hybrid nanocomposites were prepared *via* a simple, cheap, and ecological solvent casting method. FE-SEM images reveal a good dispersion of the three nanofillers within a continuous matrix. FT-IR spectra corroborate the strong interactions among the nanocomposite components *via* hydrogen bonding. A synergistic stabilization effect is observed in the hybrids, showing an unprecedented increase in the temperature of maximum rate of weight loss of 125 °C. A very strong reduction in the water vapor permeability and oxygen permeability is also observed for the nanocomposite with 1 wt% CNT, 2 wt% SEP and 2 wt% WS_2. Further, two regression methods and different machine learning approaches, namely support vector regression (SVR), support vector machines (SVM), artificial neural networks (ANNs), decision tree (DT) and random forest (RF) have been applied to predict their properties. The correlation coefficient, mean absolute error and mean square error are used as statistical indicators to compare their performance. The best models to predict the barrier properties are ANNs and SVR, while for thermal properties, SVM for classification and SVR for regression showed the most reliable performance. This triple filler strategy is a novel approach to develop hybrid nanocomposites for use in biomedicine or the food packing industry.

Received 24th September 2025,
Accepted 12th January 2026

DOI: 10.1039/d5nj03812j

rsc.li/njc

1. Introduction

Polyhydroxyalkanoates (PHAs), stored as bacterial reserve materials for carbon and energy, are a family of fully biodegradable polyesters that represent a suitable alternative to fossil fuel plastics. Many PHAs have been described, with a wide range of properties, and have countless applications in the food packaging industry, agriculture and the biomedical sector.[1] PHAs have reduced environmental impact than conventional plastics such as poly(lactic acid) (PLA), high-density polyethylene (HDPE) or polypropylene (PP). Thus, PLA polymerization of biologically produced lactic acid occurs *via* chemical processes (dimerization, ring opening polymerization), which requires synthetic, expensive, and often hazardous catalysts.[2] The most explored PHA is poly(3-hydroxybutyrate) (P3HB), that has properties comparable to those of synthetic plastics. This biopolymer is optically active, has fast biodegradation rate, high crystallinity and stability to UV radiation, and can be processed by extrusion, injection, blowing and thermoforming.[3] Though, it is brittle, has poor impact resistance, low thermal stability, narrow processing window and elevated water vapor permeability.[4] To face these issues, it can be reinforced with nanomaterials such as carbon nanotubes (CNTs) and inorganic nanoparticles or nanoclays.[4,5]

CNTs are a hollow cylindrical form of carbon allotrope with outstanding mechanical, electrical and thermal properties that make them suitable for a comprehensive range of uses.[6–8] They present very high thermal conductivity, up to 6000 W m^{-1} K^{-1} and can stand temperatures up to 700 °C in air and up to 2000 °C under inert atmosphere.[6] Further, their high specific surface area (*e.g.* 800–1100 m^2 g^{-1}) make them ideal candidates to improve the barrier properties of polymeric materials. The electrical conductivity of CNTs ranges from metallic to semiconducting based on the diameter and the rolling angle. Both noncovalent and covalent functionalization of CNTs with

[a] Universidad de Alcalá, Facultad de Ciencias, Departamento de Química Analítica, Química Física e Ingeniería Química, Ctra. Madrid-Barcelona Km. 33.6, 28805 Alcalá de Henares, Madrid, Spain. E-mail: am.diez@uah.es
[b] Departamento de Ingeniería Química y Textil, Universidad de Salamanca, Pza. Caídos 1-5, 37008 Salamanca, Spain

surfactant molecules and polymers have been widely examined.[9,10] These functionalization strategies enhance their dispersion state within the matrix, making them appropriate for numerous applications. Some concerns have arisen regarding the potential for CNTs to be hazardous to health if inhaled. This topic has been extensively investigated, but no clear conclusion has been reached yet. They cannot be classified as hazardous since insufficient data is available. The carcinogenic potential of carbon nanotubes is determined by numerous factors, including the length of the individual tubes, diameter, type, synthesis method, aggregation state, to mention but a few.[11] On the other hand, CNTs can easily be made biodegradable *via* functionalization (*e.g.* oxidation) followed by an enzymatic oxidation process.[12]

Nanoclays (NC) are nanoparticles of layered mineral silicates that hold exceptional mechanical properties. Their stability, swelling capacity, interlayer spacing, and high chemical reactivity make them ideal candidates for nanocomposite reinforcement. Amongst the most used is sepiolite (Sep), a natural hydrated magnesium-rich silicate with fibre-shaped crystalline morphology. The fibers typically are 2–10 μm long and their diameter is in the range of 10–12 nm.[13] Sep shows a high adsorption ability, very high specific surface area (close to 300 $m^2 g^{-1}$), is thermally stable up to 800 °C under air atmosphere, is highly porous, has a viscosity in the range of 2000–6000 mPa s and a Young's modulus close to 50 GPa, hence has been widely used as strengthening filler to enhance the mechanical properties of polymeric nanocomposites.[14] It has very high density of silanol groups, which enables the formation of hydrogen bonds and van der Waals interactions with other molecules and polymers.

2D materials of tungsten disulfide (WS_2) nanosheets, which are considered the most prominent members of the transition metal dichalcogenides family due to their outstanding optical and electronic properties, have recently brought a lot of attention owing to unique features such as high stability, good mechanical properties and lubricant characteristics.[15] Further, they have been reported to be low toxic and highly biocompatible. They are rapidly excreted and biodegradable.[16] They have also been extensively applied in tailoring polymer multifunction performances taking advantage of their semiconducting nature and high modulus and https://www.sciencedirect.com/topics/materials-science/mechanical-strength strength. In addition to the usual layered structure, WS_2 can also form fullerene and nanotube like geometries. Even though WS_2 shows enhanced properties, very limited literature is available, which makes it more promising towards the fabrication of superior polymer composites.[17]

Hybridization of WS_2 with other nanofillers such as CNTs provides superior mechanical, electrical and photonic properties for various applications. The combination of two or more fillers as reinforcement in a polymer matrix usually results in better properties than the sum of the individual components due to synergic effects.[18,19] Several studies dealing with the preparation of sustainable and lighter hybrid nanocomposites have been reported.[20] For instance, Saha and Kumar[21] developed epoxy/wood/graphene nanoparticle (GNP) hybrids. The addition of 5 wt% wood and 0.75 wt% GNP led to 42% tensile strength increment and 22.5% increase in impact strength. The same research group developed hemp fiber/AgNP/epoxy bionanocomposites and found about 25% increase in tensile strength upon addition of 7.5 wt% hemp and 40 wt% AgNP.[22] Further, P3HB/graphene/carbon nanofiber hybrids have already been developed as sustainable materials with enhanced mechanical properties.[4]

Artificial intelligence (AI) is one of the branches of computer science that deals with creating intelligent machines and robots to imitate human cognitive abilities and can be used to systematize a wide range of tasks, improve decision-making, and enhance the overall performance of various operations.[23] Machine learning (ML) is one of the types of AI that allows machines to learn and progress automatically *via* experience and data, and comprises three subtypes: (I) supervised learning, in which the algorithm learns from labelled examples, where it is provided with a training data set with desired inputs and outputs. Two frequent techniques are regression and classification. (II) Unsupervised learning, in which the algorithm learns from unlabeled data and looks for hidden patterns or structures in it. Two important techniques are clustering and reduction.[24] (III) Reinforcement learning, which is a combination of both types described above.

In the field of polymeric composites, ML algorithms can be applied at various stages, from the composite design to the final property characterization.[25] The use of ML to predict the properties of polymer nanocomposites based on their composition and structure is an encouraging strategy in materials science. ML models can use different methods, such as regression, classification, or deep learning, based on the nature and difficulty of the data.[26] For example, Paltakari and his group[27] applied artificial neural network (ANN), random forest (RF) and multiple linear regression (MLR) algorithms to predict the mechanical properties of nanocomposite films consisting of polyvinyl alcohol (PVA) crosslinked cellulose nanofibers and either ammonium zirconium carbonate (AZC) or glyoxal (Gx). Overall, MLR performed with least accuracy, whereas ANN prediction displayed the lowest error followed by RF. Additionally, the physically or/and chemically crosslinked hybrid films with optimized amount of crosslinkers resulted in structures with a strength to rupture that was significantly higher than that of the pure nanocellulose films. Similarly, Mahakur *et al.*[28] applied ML algorithms such as ANN, K nearest neighbors (KNN) and support vector machine (SVM) to anticipate the tribological behaviour of sustainable silane-modified jute particles/epoxy bionanocomposites with particle loading in the range of 0–12.5 wt%. The SVM model showed the best performance with a maximal coefficient of determination R^2 value of 0.9334, and minimum squared errors (MSE), and mean absolute errors (MAE) of 0.0006 and 0.019, respectively. The other models also anticipated well the coefficient of friction of the nanocomposites.

The mechanical properties of high-density polyethylene (HDPE) nanocomposites reinforced with nanodiamond were accurately predicted by an ANN model,[29] with a correlation coefficient higher than 0.99, and those of epoxy-based nanocomposites reinforced with graphene showed absolute errors lower than 1%.[30] Further, average relative errors of 0.07 were

attained for the estimation of the mechanical properties of polymeric nanocomposites reinforced with halloysite.[31] The former studies indicate that ML methods, such as ANN, can be effective in modeling the mechanical properties of nanocomposites. Though, studies on this matter are still scarce, and much research needs to be done to fully apply the potential of these methods in the field of materials science.

In the current work, a P3HB matrix has been reinforced with different amounts of two inorganic nanofillers, Sep and WS_2, as well as a carbon-based nanofiller, CNTs, *via* a simple, inexpensive, and environmentally friendly solution casting method. The main aim is to assess whether the simultaneous incorporation of three nanofillers is effective in enhancing the matrix performance *via* synergistic effects. To the best of our knowledge, no previous paper based on this triple filler strategy has been reported to improve the thermal and barrier properties of biopolymers. By adjusting the percentages of the three nanofillers, the properties could be precisely tunned to be used in targeted applications such as bioplastic food containers. Another goal of this study is to find out whether ML algorithms are suitable to accurately anticipate the properties of these hybrid polymer nanocomposites. No earlier work on the modeling of the barrier performance of multiscale hybrid polymeric nanocomposites has been published earlier.

2. Methodology

Multiple linear regression (MLR), polynomial regression, and five types of ML regression models, namely decision tree (DT), random forest (RF), artificial neural network (ANN), support vector machine (SVM) and support vector regression (SVR) have been applied to predict the properties of the hybrid nanocomposites. These algorithms are widely used in material science due to their high predictive accuracy and flexibility.[26] They were selected according to their capacity to handle non-linear data, generalization ability and enhanced accuracy. Their most important characteristics are briefly summarized below.

For the calculations, the chemical composition of the polymer nanocomposites was used as input data, and the specific thermal or barrier properties as output. Each system comprises three input variables related to the chemical composition of the nanocomposites (Sep, CNT, and WS_2), and one output variable representing a property, such as water vapor permeability, oxygen permeability, *etc.* The goal is to predict the properties as a function of the chemical composition. Given the limited size of the experimental dataset (35 samples), model evaluation and hyperparameter optimization were performed using resampling-based validation techniques rather than fixed data splits. In particular, k-fold cross-validation (k = 5) combined with grid search was employed throughout this work. This approach allows all available samples to be efficiently reused for both training and validation, while providing a statistically robust estimate of model performance and generalization in small-data scenarios. In this case, cross-validation fulfils the role of a validation procedure, while the grid search performed within each cross-validation loop acts as an internal validation step for hyperparameter selection (nested cross-validation). This strategy is widely adopted in materials and chemical sciences when experimental data are scarce, as it avoids the instability and loss of information associated with splitting small datasets into independent training, validation, and test subsets.[32] The implementation of the models has been carried out in Python v.3.12.3 using the Scikit-learn 1.7.0, Keras v.3.10.0 and TensorFlow v.2.18.1 libraries.

MLR is a statistical technique that uses several explanatory variables to predict the outcome of a response variable. It assumes there is a linear relationship between the dependent and independent variables, that the independent variables are not highly correlated, and that the variance of the residuals is constant. The coefficient of determination (R-squared) is a statistical metric used to measure how much of the variation in outcome can be explained by the variation in independent variables. R^2 increases as more predictors are added to the MLR model, even though the predictors may not be related to the outcome variable. R^2 varies between 0 and 1, where 0 indicates that the outcome cannot be predicted by any of the independent variables and 1 indicates that the outcome can be predicted without error.

A DT is a supervised learning algorithm used for classification and regression modeling, to either classify data or predict what will come next.[33] It appears as a flowchart, starting at the root node with a certain question of data, that leads to branches that hold potential answers. The branches then lead to decision (internal) nodes, which ask more questions that lead to more outcomes. This goes on until the data reaches a terminal (or "leaf") node and ends (Fig. S1).

In regression DTs, data are divided according to specific values to predict a target-continuous variable.[34] The regression DT follows the same structure as a conventional decision tree, where each internal node represents a feature, and each branch represents a possible choice or value of that feature.

Hyperparameters are adjustable settings that rule the behaviour of the tree during the training process. The key hyparameters for classifier optimization are: (I) criterion, function that measures the quality of a split in the tree nodes. The most common is the mean squared error (MSE), which assesses the average of the squared differences between predicted values and actual target values. (II) Max_depth, which controls the maximum depth or levels that the tree can grow during the training process. It determines the number of decision nodes or splits allowed in the tree before it stops dividing the data further. (III) Min_samples_split, the minimum number of samples to split an internal node. Adding min_samples_split regularizes the tree and prevents overfitting by ensuring that a minimum number of samples are present when the split occurs. (IV) Min_samples_leaf, the minimum number of samples required for internal node subdivision. Adjusting this hyperparameter can affect the generalization ability of the tree. (V) Max_leaf nodes, the maximum number of possible leaf nodes. (VII) Max_features, which represents the number of features to consider when looking for the best split at each

node in the DT. Hyperparameters are fixed before the training process and affect the structure and behavior of the tree.[35]

Artificial neural network (ANN) is a computational model inspired by the human brain's neural structure is designed to mimic the way biological neural networks in the human brain function. It is composed of multiple layers of neurons (Fig. S2): the input layer, hidden layers, and the output layer.[36] Each neuron in a layer is connected to neurons in the subsequent layer through weighted connections. The weights of these connections are adjusted during the training process to minimize errors in the network's predictions or classifications.[37]

The input layer receives raw data, which is then passed through the network, with each neuron applying an activation function to its input to produce an output. These outputs are then transmitted to the next layer, where further processing occurs. The hidden layers, which can consist of multiple layers, are where the network learns to recognize patterns and relationships in the data. The final layer, the output layer, produces the network's prediction or decision.

The process of training an ANN involves feeding it with a large dataset and using an algorithm such as backpropagation to adjust the weights of the connections based on the errors between the predicted outputs and the actual labels in the training data. This iterative process allows the network to learn from the data and improve its accuracy over time. There are several different architectures for ANNs, each with their own strengths and weaknesses.[37] The most frequent architectures are: feedforward neural networks (FNN), in which the information flows in one direction from input to output.[38] The layers are fully connected, meaning each neuron in a layer is connected to all the neurons in the next layer. Recurrent neural networks (RNNs), which have a "memory" component, where information can flow in cycles through the network.[39] This allows the network to process sequences of data, such as time series or speech. Convolutional neural networks (CNNs), which are designed to process data with a grid-like topology, such as images.[40] The layers consist of convolutional layers, which learn to detect specific features in the data, and pooling layers, which reduce the spatial dimensions of the data. Generative adversarial networks (GANs), which are used for generative modeling. They consist of two parts: a generator that learns to generate new data samples, and a discriminator that learns to distinguish between real and generated data.

In this study, the neural network consists of an input layer with three neurons, which represent the three input variables, hidden layers whose number can vary depending on the problem being addressed, and finally an output layer with a single neuron for the output variable. The hidden layers use the ReLU activation function, a common choice in feedforward artificial neural networks[41] due to its non-linearity and computational efficiency. The training is performed using the Adam optimizer with a default learning rate, and the number of epochs is set to 50. These parameters can be adjusted depending on the complexity of the problem and the network architecture. To avoid overfitting and improve generalization, dropout and L2 regularization are applied during training. The number of layers and neurons per layer is tuned *via* a grid search, reflecting a trial-and-error approach adapted to the specific task.

A support vector machine (SVM) classifies data by finding the optimal hyperplane that maximizes the margin between the closest data points of opposite classes (Fig. S3). The number of features in the input data determine if the hyperplane is a line in a 2D space or a plane in an N-dimensional space.[42] Since multiple hyperplanes can be found to differentiate classes, maximizing the margin between points enables the algorithm to find the best decision boundary between classes. This, in turn, enables it to generalize well to new data and make accurate classification predictions. The lines that are adjacent to the optimal hyperplane are known as support vectors as these vectors run through the data points that determine the maximal margin. The final SVM model is only related to support vectors.

The SVM can handle both linear and nonlinear classification tasks.[43] However, when the data is not linearly separable, kernel functions are used to transform the data higher-dimensional space to enable linear separation. This application of kernel functions can be known as the "kernel trick", and the choice of kernel function, such as linear kernels, polynomial kernels, radial basis function (RBF) kernels, or sigmoid kernels, depends on data characteristics and the specific use case. The principal hyperparameters to be modified are:[44] the Kernel parameter, which decides the function used to convert the input data into a higher dimensional space. This study applied RBF, a non-linear function commonly used in regression problems in which the data have a non-linear structure. The regularization parameter C, which governs the trade-off between model complexity and the model's ability to fit the training data. Gamma, which determines the shape of the kernel function and has a noteworthy impact on the accuracy and performance of the model. Epsilon, the error tolerance parameter that controls the margin around the regression hyperplane.

SVR is a type of SVM but is used for regression tasks. It aims to find a function that approximates the relationship between input features and continuous output values, though SVM produces discrete class labels (*e.g.*, 0 or 1 for binary classification). While SVM maximizes the margin between the support vectors of different classes, SVR tries to fit as many data points as possible within a specified margin of tolerance (epsilon) and simultaneously minimizing the model complexity.[45] SVM uses hinge loss for classification, which penalizes misclassified points, and SVR uses epsilon-insensitive loss, which ignores errors that fall within a certain distance (epsilon) from the true values. Both SVM and SVR can utilize the kernel trick to handle non-linear relationships, allowing them to operate in high-dimensional spaces.

3. Experimental

3.1 Materials

Poly(3-hydroxybutyrate) (P3HB), with an average molecular weight of 80 000 g moL^{-1}, glass transition temperature $T_g \sim 20$ °C, melting temperature of 174 °C and $d_{25°C} = 1.26$ g cm^{-3} was supplied by Biomer Ltd (Germany). Carbon nanotubes

(CNTs), with an outer average diameter of 20–40 nm, length ranging from 0.5 to 1 μm and purity of 97% were supplied by Nanothinx (Greece). Tungsten disulfide (WS_2) nanosheets prepared by the surfactant exfoliation method, with thicknesses in the range of 1–5 nm and $d_{25°C}$ = 7.50 g cm^{-3} were obtained from XFNANO Materials Tech Co., Ltd (China). Sepiolite (Sep) nanoclay, with a purity of 95%, $d_{25°C}$ = 1.26 g cm^{-3} and specific surface area in the range of 220–270 m^2 g^{-1}, was provided by Sigma-Aldrich (Spain). All the reagents were of analytical grade and used as received.

3.2 Nanocomposite preparation

The hybrid nanocomposites were manufactured through solution casting, as shown in Fig. 1. Firstly, the CNTs were dispersed in chloroform *via* sonication for 20 min. Independently, Sep was dispersed in water by sonication for 10 min and then mixed with the CNT dispersion, which was sonicated for another 60 min. Then, the WS_2 nanosheets were added and sonicated once again for 30 min. Subsequently, PHB was mixed with the former dispersion, which was sonicated for another 60 min. The resulting mixture was then cast onto a glass Petri dish and dried for 48 h to attain homogeneous films. The loading of each nanofiller was varied between 0 and 5 wt%, so that the total nanofiller loading was $\leq$5 for all the samples. This concentration range was selected based on preliminary studies that indicated a high degree of agglomeration for higher loadings. The sample containing 1 wt% of SEP, CNT and WS_2 was prepared three times to check for reproducibility. A small batch-to-batch variability was found.

3.3 Characterization techniques

The surface morphology of cryofractured surfaces of the nanocomposites was studied by field-emission scanning electron microscopy (FE-SEM) using a Sigma 360-VP microscope (Zeiss, Germany) coupled with an EDAX (energy-dispersive X-ray spectroscopy) detector to corroborate the sample composition. The nanocomposites were sputtered with a 10 nm-thick gold layer to avoid charging during electron irradiation. Experiments were performed under high vacuum to avoid interferences from secondary and backscattered electrons, at an acceleration voltage of 25 kV, probe current of 35 pA and titling angle of 0 °C, at magnifications from ×200 to ×10 000. Images were analyzed by Fiji/ImageJ2 (version 2.3.0) open-source software to determine mean sizes and related standard deviations.

Infrared spectroscopy (FT-IR) experiments were performed with a Spectrum Two Spectrometer (PerkinElmer, USA) equipped with a diamond crystal in attenuated total reflectance (ATR) mode. Measurements were carried out in the range of 4000–400 cm^{-1} at room temperature, with a spectral resolution of 4 cm^{-1} and 64 scans for each spectrum.

The thermal stability was assessed using a Q 500 thermogravimetric analyzer (TA Instruments, USA), according to ASTM E1868-10. Five samples for each nanocomposite were evaluated with a 10 °C per minute ramp, ranging from 20 °C to 800 °C under a nitrogen atmosphere, with a gas flow of 60 mL min^{-1}. Initial sample weights varied from 10 mg to 15 mg. The initial degradation temperature (T_{onset}) was determined at 2% mass loss, and the temperature of maximum rate of degradation (T_{max}) was calculated as the maximum of the first derivative.

Water vapor permeability (WVP) was determined using the gravimetric method following the ASTM E96-95 standard. Samples were placed in Payne permeability cups (Elcometer SPRL, Belgium). Distilled water was placed inside the cups to expose the film to 100% RH on one side. The cups were weighed periodically (±0.0001 g) and equilibrated at 25 °C and 54% RH. WVP was calculated using the equation: WVP = $(\Delta ml)/(At\Delta P)$, in which Δm is the weight loss of each cup, l the film thickness, t the time, A the contact area and ΔP the partial pressure difference between inside and outside of the cup. Experiments were performed in quadruplicate and average values are reported.

Oxygen permeability (OP) was calculated *via* measuring the oxygen transference rate (OTR) with a C130H gas permeability tester (Labthink GmbH, Germany), following the ASTM D3985-05 standard. Experiments were carried out at 25 °C and 54% RH. The samples were previously purged with nitrogen in the humidity equilibrated samples, before exposure to an oxygen flow of 10 mL min^{-1}. OP was calculated following the expression: OP = (OTR l)/ΔP, where l is the average film thickness and ΔP the difference between oxygen partial pressure across the film. Experiments were performed in triplicate and average values are reported.

4. Results and discussion

4.1 Fractography analysis

To get more information about the surface morphology of the nanocomposites, cryofractured specimens were observed *via*

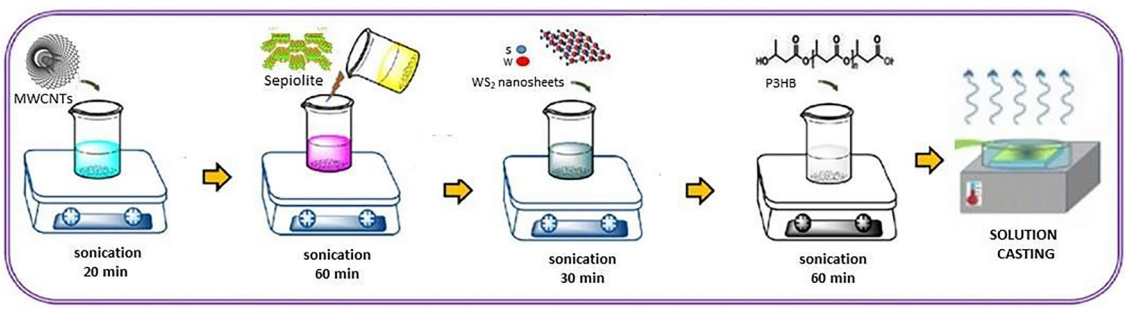

Fig. 1 Representation of the synthesis of PHB/Sep/CNT/WS_2 hybrid nanocomposites *via* sonication followed by solution casting.

SEM, and representative images of nanocomposites with 2 : 1 : 2 and 1 : 1 : 1 (Sep/CNT/WS_2) loading at different magnifications are shown in Fig. 2. Analogous micrographs were observed for the other hybrid composites. Both nanocomposites show a good dispersion of the three nanofillers, which are found to be homogenously and randomly dispersed within a continuous matrix with low degree of porosity (Fig. 2a and b). This improved dispersion supports the improvements in thermal stability and barrier performance compared to the P3HB matrix, as will be discussed in the following sections. Further, the homogenous filler distribution minimizes the stress concentration nuclei, which will be a leading cause of premature failure, in agreement with previous works on hybrid nanocomposites.[46,47] In the images at higher magnification (Fig. 2c), a dense and entangled network of sepiolite nanofibers in between the CNTs can be observed. The nanoclay acts as a stabilizer, reducing the van der Waals interactions between the CNTs, thus preventing their aggregation.

A close examination of the images reveals some differences in the fracture behaviour of the two composites. Thus, in the one with 2 : 1 : 2 (Sep/CNT/WS_2) loading, significant crack propagation can be observed (Fig. 2a). This can be explained considering that the higher the total nanofiller loading, the stronger the interactions among them, as evidenced in the higher magnification image (Fig. 2c), and these would weak the interfacial adhesion with the matrix. Further, the formation of a dense nanofiller network confines the ductile flow of the polymer, and this is reflected in earlier failure, hence will lead to poor impact resistance. Similar behaviour has been reported for PEEK nanocomposites filled with graphene and Ti nanoparticles,[48] in which the nanofillers decrease the flowability of PEEK matrix, resulting in a reduction of impact strength. In contrast, in the sample with 1 : 1 : 1 (Sep/CNT/WS_2) loading, different toughening mechanisms can be observed: crack deflection, CNTs bridging and CNTs pull-out. Thus, the CNTs can act as effective barriers for pinning and bifurcation of the advancing cracks. Further, the CNTs pull out prevents localization of the stresses, and this typically results in a better impact resistance.

4.2 Thermal stability of PHB-based nanocomposites

The thermal stability was assessed *via* TGA, and the thermograms of the ternary composites are shown in Fig. 3. For comparison, the data of the neat components are also included. TGA data for all the samples developed in this work are collected in Table S1. Neat PHB shows a single decomposition stage that initiates (T_{onset}) at ~178 °C and shows the maximum rate of weight loss (T_{max}) at around 220 °C. The degradation takes place *via* chain scission mechanism, by a random *cis*-elimination reaction at a six-membered ring ester intermediate, producing unsaturated carboxyl acid and ester products.[3] The CNTs and WS_2 nanosheets display very high thermal stability,

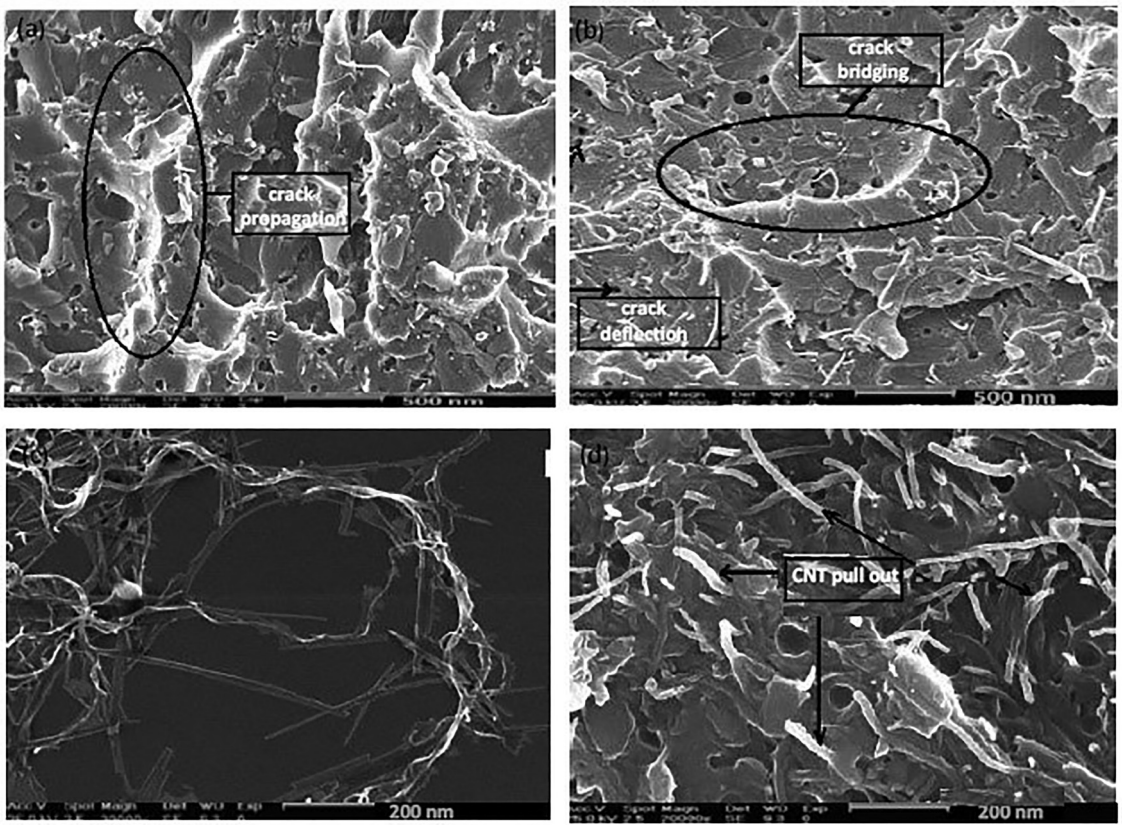

Fig. 2 SEM images from fractured specimens of P3HB/Sep (2.0 wt%)/CNT (1.0 wt%)/WS_2 (2.0 wt%) (a) and (c) and P3HB/Sep (1.0 wt%)/CNT (1.0 wt%)/WS_2 (1.0 wt%) (b) and (d) nanocomposite at different magnifications.

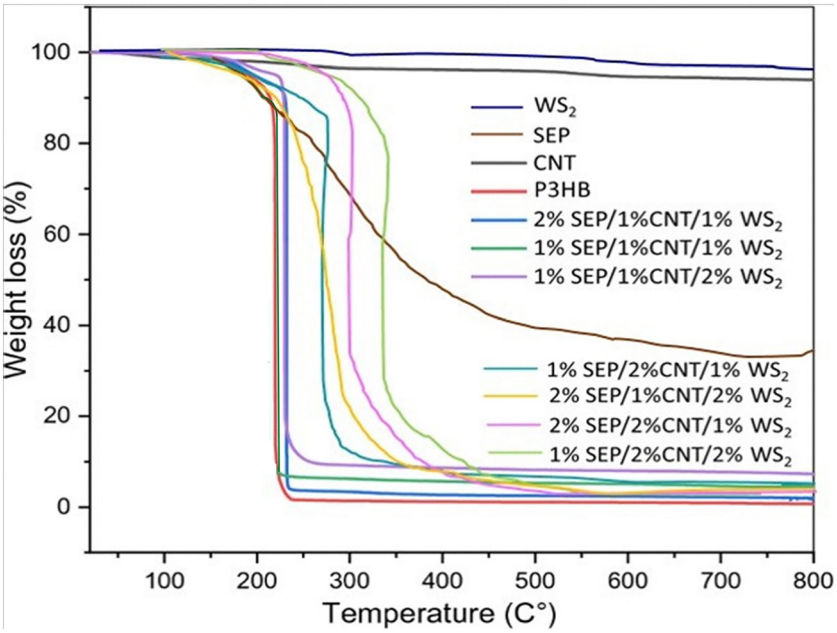

Fig. 3 TGA curves of PHB/Sep/CNT/WS_2 hybrid nanocomposites under a nitrogen atmosphere, with a gas flow of 60 mL min^{-1}.

and hardly decompose in the temperature range studied, while sepiolite losses about 40% weight in the range 150–500 °C, in agreement with results reported earlier.[49]

A one-step decomposition process is also found for the nanocomposites, although it is in general shifted to higher temperatures, indicating the outstanding thermal stability improvement caused by the presence of the three fillers. Regarding the binary composites, the largest temperature improvements (up to 60 °C in T_{10}) are found for the sample with 5 wt% CNTs, while those with the same amount of SEP or WS_2 led to increments of about 30 and 50 °C, respectively.

Indeed, a synergistic stabilization effect is observed in the hybrids, particularly those with higher loading of CNTs and WS_2, with a maximum increase in T_{max} of about 125 °C for the sample with 1% Sep, 2% CNT and 2% WS_2. Similarly, the sample with 2% Sep, 2% CNT and 1% WS_2 shows a T_{max} about 100 °C higher than that of the neat polymer, and the sample with 2% Sep, 1% CNT and 2% WS_2 shows about 80 °C increment. Regarding the T_{onset}, the increments are also very significant, the highest being close to 120 °C. These extraordinary increments, considerably higher than those reported for PHBV filled with CNTs or inorganic nanoparticles,[4,5] can be ascribed to the combination of several factors:[50,51] (I) the decrease in the free volume between polymer chains that are occupied by nanofillers; therefore, chains are much more squeezed and density increases, which would lead to an increase in the degradation activation energy. In fact, the good dispersion of the nanofillers within the matrix would promote the fillers to be overlapped and arranged more closely, resulting in a synergistic effect and a very high increase in the thermal conductivity of the hybrid nanocomposites. (II) The nanofillers can act as barriers, restraining the release of volatile products from the bulk of the matrix to the gas phase, which would be reflected in higher thermal stability. (III) CNTs could form a conductive network facilitating the phonon transfer, leading to high thermal conductivity, which can lighten the local overheating and improve the thermal stability of the nanocomposites. (IV) Formation of hydrogen bonds between the matrix and the nanofillers, especially with sepiolite nanoclay, since this hinders the homolytic chain scission. A strong synergistic effect in enhancing thermal conductivity has also been reported for other polymers reinforced with CNTs and WS_2.[15] Synergistic effects have also been reported for thermosplastics reinforced with sepiolite and CNTs, suggesting that the CNTs acted as a sealing agent to create a network with the clay fibers, forming a much tighter char than the nanoclay alone.[52] Thus, more char limits the amount of volatile gases escaping from the degrading polymer and impedes the oxygen ingress. The differences found within the hybrids seem to be directly related to the thermal conductivity of the individual components (about 2600,[51] 140[53] and 3.4 W m^{-1} K^{-1} (ref. 54) for multi-walled CNTs, WS_2 and sepiolite, respectively). Thus, for the same total nanofiller loading, the hybrids with higher sepiolite content show lower degradation temperatures. Overall, the onset degradation temperature of all the hybrids meets the requirements for their use in biomedicine or in the food packing industry.

4.3 Infrared spectroscopy

To investigate the interactions between the functional groups of the nanofillers and the matrix, an FTIR study was performed (Fig. 4). The typical bands of the polymer located at 2980–2850 cm^{-1} (alkyl–CH_3 group), 1725 cm^{-1} (C═O group), 1150–1300 cm^{-1} (–C–O–C– stretching of the ester bonds), 1020 cm^{-1} (–O–C–C– stretching vibration) and 950 cm^{-1} (–C–OH bending) are in good agreement with former studies.[3] They can also be observed in the nanocomposites, albeit some of them are shifted to lower wavenumbers. In particular, the C═O stretching is significantly shifted, by up to 50 cm^{-1} for the sample with 1% Sep, 2% CNT

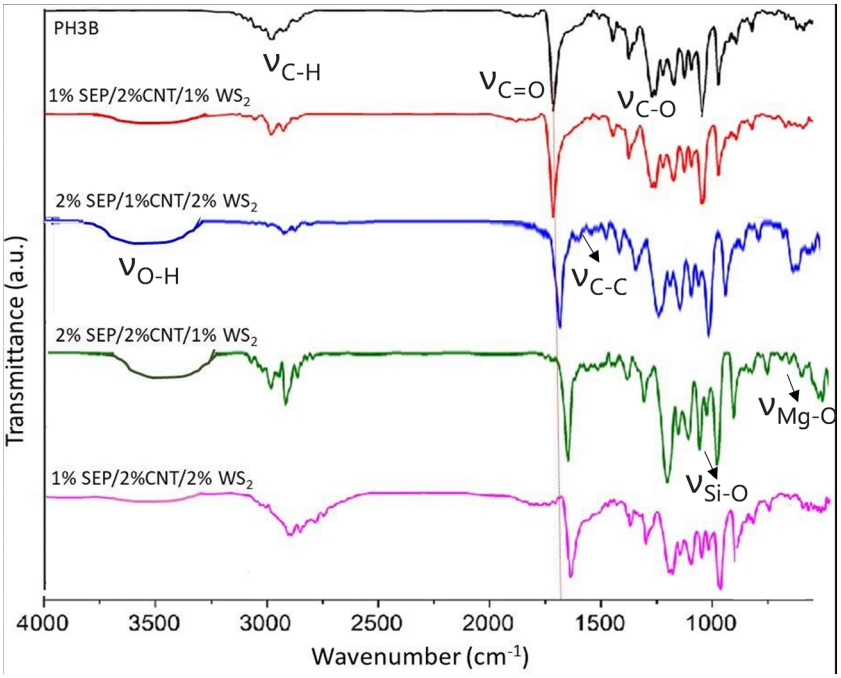

Fig. 4 Representative ATR-FTIR spectra of P3HB/Sep/CNT/WS_2 nanocomposites at room temperature, with a spectral resolution of 4 cm^{-1} and 64 scans for each spectrum.

and 2% WS_2. This strong shift is ascribed to the formation of hydrogen bonds with the OH groups of sepiolite. Thus, it has been reported that the interactions between nanofillers and polyesters lead to a broadening of the C═O stretching band and cause a downshift.[55] Further, the change in the position of this band could also be related to the change in crystallinity upon addition of the nanofillers, since its shape and position depend on the fraction of amorphous and crystalline regions.[56] It is worthy to note that the nanocomposite with the largest shift in the C═O stretching is the one with highest thermal stability, indicative that this property is conditioned by the nanofiller–matrix interactions. Moreover, the band related to the C–H stretching shifts towards lower wavenumber and shows increased intensity, which could be indicative of the existence of CH–π interactions between the CH_2 groups on P3HB chains and the sp^2 aromatic structures of the CNTs, in agreement with results reported earlier for polyester based-nanocomposites.[57] Other additional bands appear in the spectra of the nanocomposites that corroborate the strong nanofiller–matrix interactions. A new band appears in the range of 3600–3200 cm^{-1}, related to the O–H stretching of the hydroxyl groups of sepiolite. This band is also shifted to lower wavenumbers compared to that of neat sepiolite,[58] and the shift is stronger for the nacocomposites with higher sepiolite content. Further, it is more pronounced in the nanocomposite with 2% Sep, 2% CNT and 1% WS_2, which may be related to the presence of defects, that is, a small amount of OH and COOH groups in the surface of the CNTs, that hence could also be prone to interact *via* H-bonding. This is in agreement with the higher thermal stability of this composite compared to 2% Sep, 1% CNT and 2% WS_2, thus corroborating that the formation of H-bonds results in improved thermal stability.

Other bands related to sepiolite can also be observed in the spectra. The bands at about 1000 cm^{-1} correspond to symmetric stretching vibrations of Si–O–Si bonds[58] and those between 600 and 850 cm^{-1} are related to Mg–O–Mg. Further, smalls band appear at about 1580 cm^{-1} related to the aromatic rings of the CNTs. Overall, the IR spectra corroborate the strong interactions between the functional groups of the nanocomposite components.

4.4 Barrier properties

One of the principal aims when adding nanofillers to polymers is to enhance their barrier properties to gases, vapors and organic compounds to be used in food packaging.[3] The two main permeants examined for packaging applications are moisture and oxygen, which are the major causes of food spoilage, and can reduce product quality and shelf life.[59] For example, the improving of the oxygen barrier performances of a film is of great importance because oxygen promotes a lot of degradation mechanisms of a food, such as corrosive phenomena, oxidations, and great modification of organoleptic properties.[60] Thus, the water vapor permeability (WVP) and the oxygen permeability, amount of water vapor and oxygen that permeate per unit of area and time, respectively, were tested, and the results for binary and some ternary hybrids are plotted in Fig. 5. Results for all the samples are collected in Table S2. As can be observed, both parameters drop gradually with nanofiller concentration, showing a minimum value at the highest nanofiller tested. Regarding binary composites, the largest drops (about 77 and 82% for OP and WVP, respectively) are found for the nanocomposite with 5 wt% WS_2, while the same amount of CNTs just lead to 41 and 56% fall, respectively, and the same concentration of SEP resulted

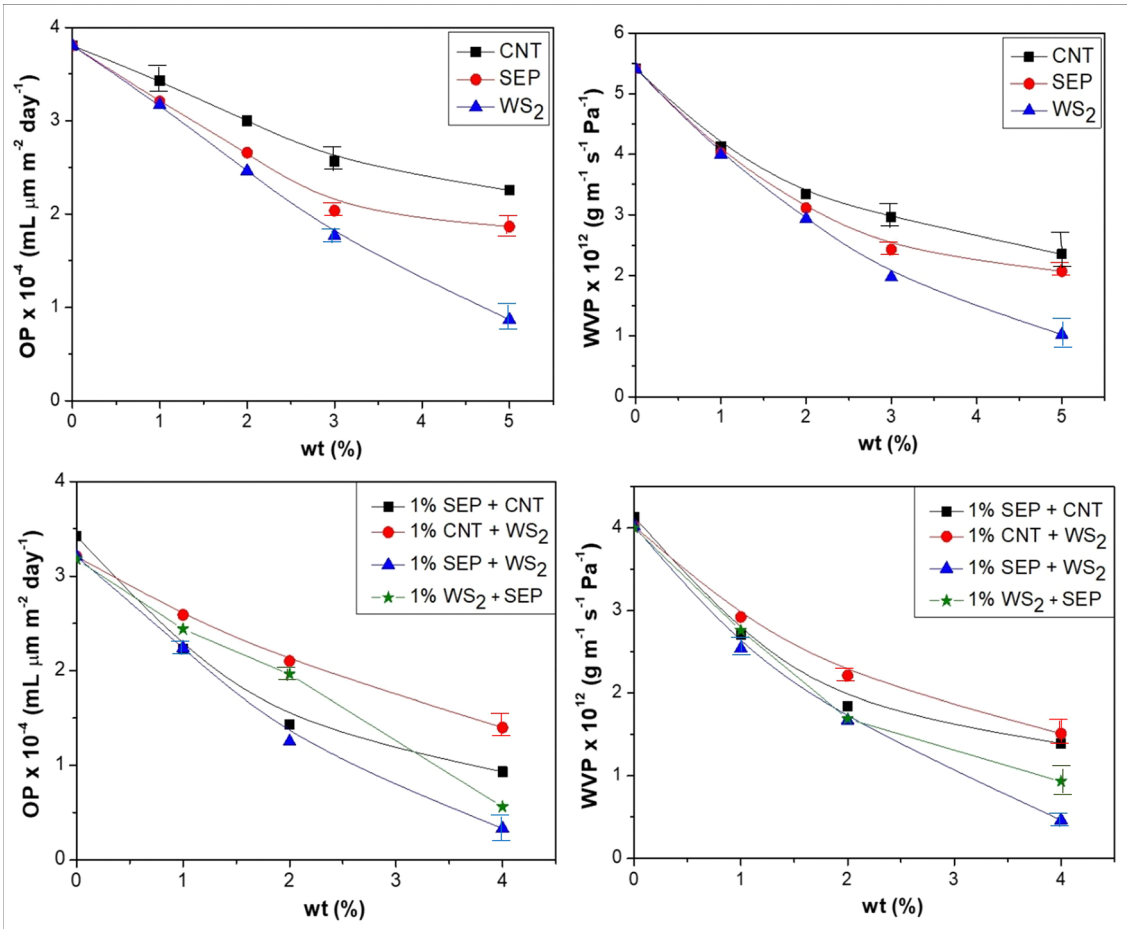

Fig. 5 Oxygen permeability (OP) and water vapor permeability (WVP) for binary P3HB/Sep, P3HB/CNT and P3HB/WS_2 nanocomposites (top) and ternary P3HB/Sep (1 wt%)/CNT, P3HB/Sep (1 wt%)/WS_2, P3HB/CNT (1 wt%)/WS_2 and P3HB/WS_2 (1 wt%)/Sep nanocomposites (down) as a function of the indicated nanofiller loading.

in 51 and 61% drop. The permeation of gas through a polymer can be described by a diffusion model, using Henry and Fick's laws.[60] The WS_2 with a layered 2D structure increases the tortuosity of the transport path, and will lead to a higher barrier effect than 1D CNTs or Sep, thus resulting in lower permeability. This is in agreement with the effect found upon addition of WS_2 to other thermoplastic matrices.[61] The improvements found herein are larger than those reported for P3HB reinforced with nanoclay[62] or graphene.[63] This improved barrier performance should be related to the very homogeneous nanofiller dispersion, its strong interfacial adhesion with the polyester matrix as revealed by the IR spectra that causes chain immobilization combined with the compactation and decrease in free volume in the nanocomposites.

Regarding ternary composites, the largest drop in OP and WVP is found upon combination of sepiolite and WS_2, up to 92% and 90%, respectively, for 4 WS_2 loading. This decrease is significantly higher than the found upon combination of CNTs and the same amount of WS_2. The improved barrier performance of sepiolite compared to CNTs has been ascribed to the exfoliation of sepiolite in the nanocomposites, creating a labyrinth effect or tortuous path.[64] Further, it has been proved that sepiolite reduces the oxygen permeability of polymer nanocomposites not only by creating a tortuous path but also *via* gas adsorption onto its surface, due to the large number of silanol groups and large cavities in its structure.[65] With regard to the quaternary hybrids (Table S2), the largest drops (95 and 93% in OP and WVP) are found for the nanocomposite with 2% Sep, 1% CNT and 2% WS_2, in agreement with the discussion above. A 93% drop in OP is also observed for that with 1% Sep, 2% CNT and 2% WS_2, indicative also of a noticeable synergic effect. Results demonstrate that the incorporation of different nanofillers to PHB matrix has a very positive effect on the gas barrier properties, leading to ideal materials for packaging oxygen- and/or moisture-sensitive products.

4.5 Modelling of the thermal and barrier properties

The modelling of thermal and barrier properties was carried out using the methods mentioned in previous sections. Due to the limited size of the available dataset, model performance was evaluated using 5-fold cross-validation combined with systematic hyperparameter exploration *via* grid search. This procedure

Table 1 Lasso regression equations

Variable	Equation
OP	$1.736 \times 10^4 - 8.219 \times 10^3 \cdot$[SEP] $-4.958 \times 10^3 \cdot$[MWCNT] $- 9.413 \times 10^3 \cdot$[WS2]
WVP	$2.059 - 1.003 \cdot$[SEP] $-0.657 \cdot$[MWCNT] $- 1.115 \cdot$[WS2]
T_{onset}	$2.086 \times 10^2 + 4.680 \cdot$[SEP] $+1.513 \times 10^1 \cdot$[MWCNT] $+ 1.287 \times 10^1 \cdot$[WS2]
T_{10}	$2.477 \times 10^2 + 3.934 \cdot$[SEP] $+1.700 \times 10^1 \cdot$[MWCNT] $+ 1.305 \times 10^1 \cdot$[WS2]
T_{max}	$2.540 \times 10^1 + 4.858 \cdot$[SEP] $+1.738 \times 10^1 \cdot$[MWCNT] $+ 1.470 \times 10^1 \cdot$[WS2]

provides an estimate of model generalization while minimizing bias and variance associated with small experimental datasets. No independent hold-out validation dataset was defined, as fixed train/validation/test splits are known to yield highly unstable and sample-dependent results when the number of available samples is small. Instead, all reported performance metrics correspond to cross-validated averages, ensuring that each experimental sample is used both for training and validation across different folds.

To apply the linear regression model, Lasso regression was used because it is a type of multivariate linear regression that helps reduce overfitting and improve performance. The alpha parameter was explored within the interval (0, 100), and a grid search with cross-validation (5 folds) was performed to obtain the average R^2 value. The results of the fitting process are presented in Tables 1 and 2, meanwhile extended results are included in Table S3.

The equations presented in Table 1 capture the qualitative effects of nanofiller addition observed in Fig. 5 for the barrier properties. On one hand, oxygen permeability (OP) exhibits negative coefficients, since the incorporation of any filler reduces its value, similarly to water vapor permeability (WVP). On the other hand, the equations related to T_{onset}, T_{10}, and T_{max} show a positive trend, since the use of nanofillers enhances the thermal properties, as illustrated in Fig. 3. The higher alpha value found for OP suggests that this variable requires stronger regularization compared to the other properties. Although the model fits the barrier properties well during training, their average test performance is poorer. In contrast, the models for thermal properties are better balanced between training and test stages.

To study the combined effect of two or more nanofillers, a polynomial regression was applied, covering degrees from 2 to 4. Similarly, a grid search with cross-validation was performed to determine the average R^2 value, which results are collected in Table S4. The results collected in Table 3 reveal two clear trends: (1) the best-performing model is the polynomial of degree 2, regardless of the property under study; and (2) the prediction of barrier properties improves considerably compared to Lasso regression, whereas the fit for thermal properties is significantly worse.

The effect of different polynomial degrees is presented in Fig. 6 for variables WVP and T_{onset}, meanwhile Fig. S4–S6 shows the predictions for T_{10}, T_{max} and OP.

Fig. 6 illustrates that increasing the polynomial degree can locally improve fitness, but it also introduces a higher risk of overfitting. At elevated degrees, the models exhibit pronounced and unrealistic deviations, including over and underestimation. This behavior is evident in the degree 4 model for WVP, which produces extreme predicted values (above 6 and below −1), as well as in the degree 3 and degree 4 models for T_{onset}, where similar instabilities are observed. Analogous results were obtained for T_{max}, T_{10}, and OP, in terms of overfitting and deviations at higher degrees.

Table 4 shows the fitted equations obtained for each property. Notably, while the barrier properties exhibit a greater influence from degree 1 terms (up to one order of magnitude larger than second-degree terms), the thermal properties show more balanced coefficients across the three equations. This is likely because the three temperature-related variables are interrelated, reflecting the degradation stages observed in TGA experiments (see Fig. 3).

SVM method was applied to classify the data into two classes. To this end, both the linear and radial basis function (RBF) kernels were used, allowing the model to address both linear and nonlinear classification tasks. The values of the regularization parameter C were explored within the interval (0, 10). The best solutions obtained are presented in Table 5, meanwhile the extended results are shown in Table S5, and the classification

Table 3 Statistical metrics of the best polynomial regression models

Variable	Degree	MSE (CV)	MAE (CV)	R^2 (CV)
OP	2	6.167×10^6	2.087×10^3	7.860×10^{-1}
WVP	2	3.070×10^{-2}	1.280×10^{-1}	9.132×10^{-1}
T_{onset}	2	3.320×10^2	1.374×10^1	-4.791×10^{-1}
T_{10}	2	3.986×10^2	1.565×10^1	-1.818×10^{-1}
T_{max}	2	8.199×10^2	2.183×10^1	-1.440

Table 2 Statistical metrics of Lasso regression model

Variable	MSE (train)	MSE (test)	MAE (train)	MAE (test)	R^2 (train)	R^2 (test)	Best alpha
OP	1.193×10^7	3.587×10^7	2.848×10^3	4.398×10^3	8.876×10^{-1}	2.697×10^{-1}	100.0
WVP	1.659×10^{-1}	5.494×10^{-1}	3.468×10^{-1}	6.096×10^{-1}	8.975×10^{-1}	2.041×10^{-1}	0.010
T_{onset}	1.968×10^2	9.242×10^1	7.827	6.898	5.548×10^{-1}	4.683×10^{-1}	0.028
T_{10}	2.055×10^2	1.003×10^2	8.676	7.788	5.987×10^{-1}	5.508×10^{-1}	0.215
T_{max}	3.388×10^2	7.377×10^1	1.170×10^1	5.748	5.746×10^{-1}	7.402×10^{-1}	0.600

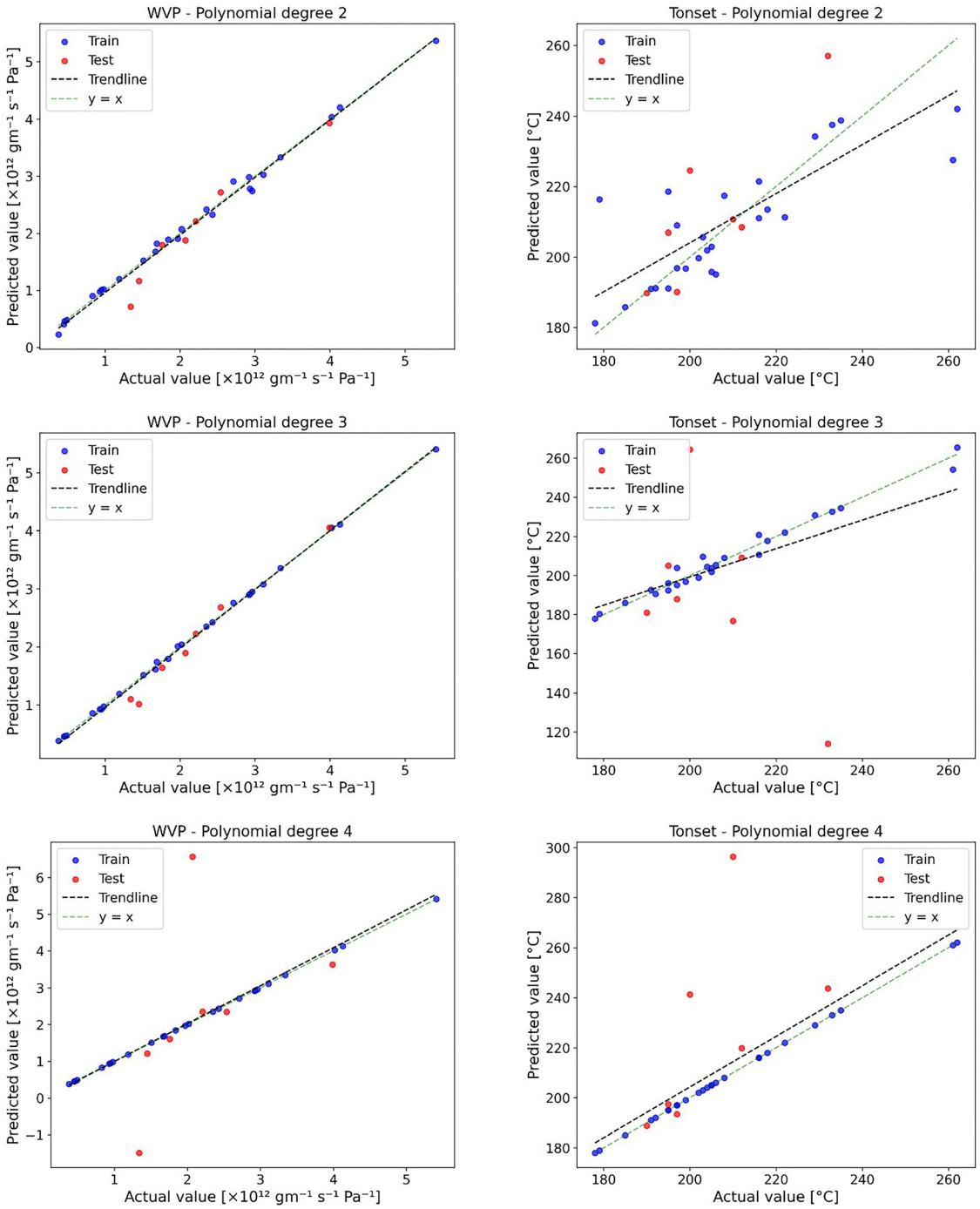

Fig. 6 Comparative representation of polynomial regression models of three degrees for water vapor permeability (WVP, left) and initial degradation temperature (T_{onset}, right). The first, second, and third rows correspond to polynomial degrees 2, 3, and 4, respectively.

results for OP, WVP, T_{onset}, and T_{max} are shown in Fig. 7 and Fig. S7.

The results show a notably high performance for the thermal variables, while the barrier properties were classified with slightly lower accuracy. For the barrier properties, both are better represented using the linear kernel, although OP required a higher penalization value ($C = 10 > 1$), to reduce prediction errors.

The F1-score asymmetry observed for WVP suggests that class 1 is easier to predict, and that classification could potentially be improved by incorporating additional parameters.

In contrast, the symmetry of the F1-scores for OP indicates that a linear decision boundary is sufficient to reasonably separate both classes.

In the case of the thermal properties, which exhibit more complex non-linear relationships, the RBF kernel provided a

Table 4 Polynomial regression equations for each variable

Variable	Equation
OP	$1.387 \times 10^4 - 9.075 \times 10^3 \cdot [\text{SEP}] - 7.411 \times 10^3 \cdot [\text{MWCNT}] - 1.204 \times 10^4 \cdot [\text{WS2}] + 7.926 \times 10^2 \cdot [\text{SEP}]^2 - 5.333 \times 10^2 \cdot [\text{SEP}] \cdot [\text{MWCNT}] - 7.391 \times 10^2 \cdot [\text{SEP}] \cdot [\text{WS2}] + 8.041 \cdot 10^2 \cdot [\text{MWCNT}]^2 - 1.017 \times 10^3 \cdot [\text{MWCNT}] \cdot [\text{WS2}] + 1.234 \times 10^3 \cdot [\text{WS2}]^2$
WVP	$1.509 - 1.133 \cdot [\text{SEP}] - 0.892 \cdot [\text{MWCNT}] - 1.298 \cdot [\text{WS2}] + 0.264 \cdot [\text{SEP}]^2 + 0.164 \cdot [\text{SEP}] \cdot [\text{MWCNT}] + 0.201 \cdot [\text{SEP}] \cdot [\text{WS2}] + 0.208 \cdot [\text{MWCNT}]^2 + 0.221 \cdot [\text{MWCNT}] \cdot [\text{WS2}] + 0.248 \cdot [\text{WS2}]^2$
T_{onset}	$2.085 \times 10^2 + 1.622 \cdot [\text{SEP}] + 2.185 \times 10^1 \cdot [\text{MWCNT}] + 1.359 \times 10^1 \cdot [\text{WS2}] + 0.562 \cdot [\text{SEP}]^2 + 1.551 \cdot [\text{SEP}] \cdot [\text{MWCNT}] - 7.193 \cdot [\text{SEP}] \cdot [\text{WS2}] + 0.562 \cdot [\text{MWCNT}]^2 + 9.352 \cdot [\text{MWCNT}] \cdot [\text{WS2}] + 1.168 \cdot [\text{WS2}]^2$
T_{10}	$2.485 \times 10^2 + 2.780 \cdot [\text{SEP}] + 2.677 \times 10^1 \cdot [\text{MWCNT}] + 1.609 \times 10^1 \cdot [\text{WS2}] + 8.090 \times 10^{-2} \cdot [\text{SEP}]^2 + 2.263 \cdot [\text{SEP}] \cdot [\text{MWCNT}] - 3.403 \cdot [\text{SEP}] \cdot [\text{WS2}] + 0.811 \cdot [\text{MWCNT}]^2 + 1.463 \times 10^1 \cdot [\text{MWCNT}] \cdot [\text{WS2}] + 3.285 \cdot [\text{WS2}]^2$
T_{max}	$2.588 \times 10^2 + 9.413 \cdot [\text{SEP}] + 3.702 \times 10^1 \cdot [\text{MWCNT}] + 2.879 \times 10^1 \cdot [\text{WS2}] + 1.262 \times 10^{-1} \cdot [\text{SEP}]^2 + 5.080 \cdot [\text{SEP}] \cdot [\text{MWCNT}] + 4.822 \cdot [\text{SEP}] \cdot [\text{WS2}] + 1.560 \cdot [\text{MWCNT}]^2 + 2.688 \times 10^1 \cdot [\text{MWCNT}] \cdot [\text{WS2}] + 5.307 \cdot [\text{WS2}]^2$

Table 5 Best solutions obtained for SVM method

Variable	Best parameters	Accuracy	F1-score (class 0)	F1-score (class 1)
OP	{'C': 10, 'kernel': 'linear'}	0.847	0.847	0.847
WVP	{'C': 1, 'kernel': 'linear'}	0.714	0.667	0.750
T_{onset}	{'C': 10, 'kernel': 'rbf'}	0.847	0.847	0.847
T_{10}	{'C': 10, 'kernel': 'rbf'}	1	1	1
T_{max}	{'C': 1, 'kernel': 'rbf'}	1	1	1

better fit. Unlike the barrier properties, the F1-scores for the thermal variables are balanced and robust in all cases. While T_{onset} and T_{10} required stronger regularization to separate the classes compared to T_{max}, all three thermal variables were classified successfully.

To apply the SVR method to the experimental data, the values of the regularization parameter C = (0.1, 1, 10, 100) and the tolerance margin ε = (0.01, 0.1, 0.5, 1) were considered. The best solutions obtained are displayed in Table 6, and the full set of mean solutions is included in Table S6.

The prediction of barrier properties shares both the same C and ε values for WVP and OP, aiming to minimize the error by using the maximum C and minimum ε. In this case, WVP can be predicted with a very accurate and stable model (high R^2, very low MSE and MAE), while OP displays extremely high error values. This may be due to the model treating the OP data primarily as outliers, or due to overfitting, caused by the aggressive parameter setting (high C, low ε).

For the thermal properties, increasing ε allowed for a reduction in the value of C, resulting in more generalized models for both T_{onset} and T_{10}. However, T_{max} required a higher penalization of errors, which led to clear overfitting in the test set compared to the training set.

For the formulation of the ANNs, various numbers of hidden layers were considered and optimized, layers = (1, 2, 3, 4, 5, 6), along with a range of possible neurons per layer, neurons = (10, 20, 30, 40, 50, 60, 70, 80, 90, 100, 110, 120). The values for the number of epochs and batch size were kept constant across all cases. The results are presented in Table 7. In general, it can be stated that the barrier properties exhibit better predictive performance than the thermal properties when using the same ANN configurations.

The modelling applied to OP is able to explain most of the variance in both the training and testets, although it required a deep architecture (6 layers with 100 neurons each) to achieve such results. In contrast, WVP shows a more balanced fit between training and test, as well as a much lower MAE, and it achieved this with the simplest architecture among all the properties studied. Fig. 8 illustrates how the different parameter combinations (folds) explored for the ANN minimize the MSE to a nearly convergent value starting from a 2-layer architecture (with fold counts between 60 and 120).

On the other hand, the thermal properties did not achieve acceptable performance under any of the evaluation metrics. Moreover, they were predominantly associated with complex network architectures that failed to either generalize or learn effectively.

DT method was applied using the following hyperparameters: maximum depths were considered as Max_depth = (none, 3, 5, 10); the minimum number of samples required to split a node was set as Min_samples_split (2, 5, 10); the minimum number of samples per leaf as Min_samples_leaf = (1, 5, 10); and the number of features considered for each split as Max_features = (none, sqrt, log2). The results of the best performing configurations are presented in Table 8.

Most of the models showed very poor performance in both training and validation, with negative R^2 values, indicating that they were unable to outperform a simple mean prediction. The high MSE and MAE values confirm that the predictions were highly inaccurate, even when tree depths were set to 5 or 10. Only the variable WVP achieved a marginally acceptable performance, with a test R^2 of 0.07, suggesting that the model was able to extract a small amount of useful information.

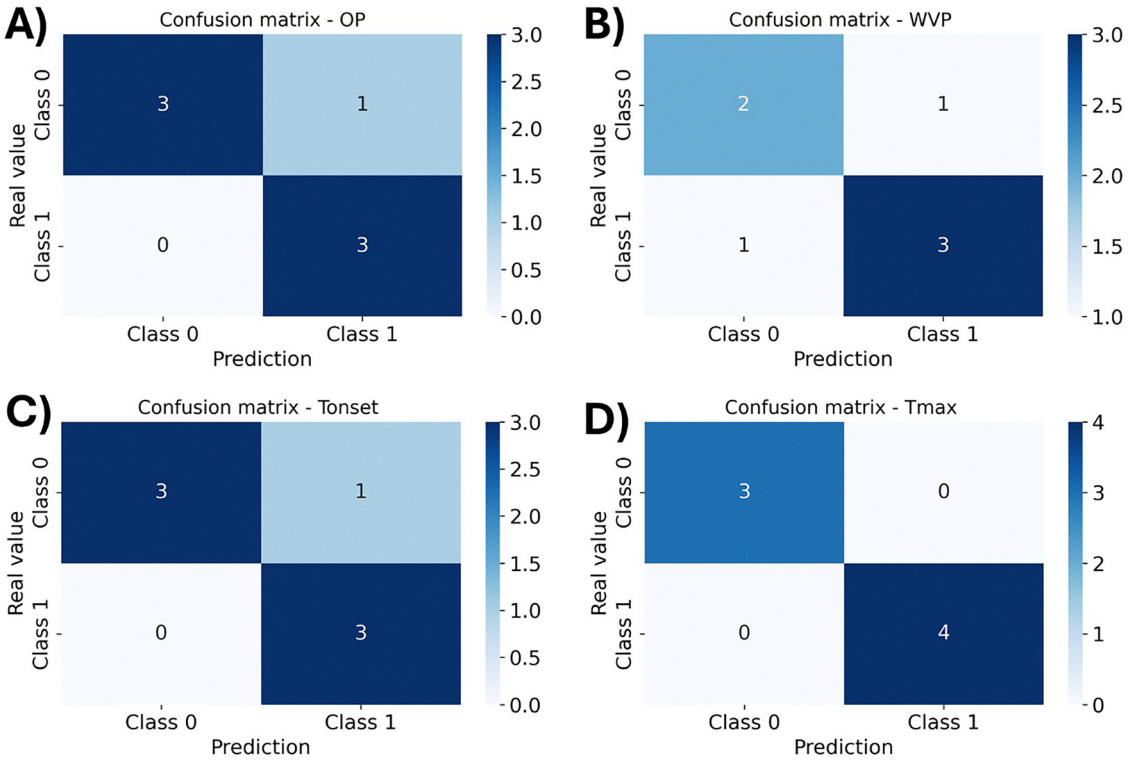

Fig. 7 Confusion matrices for support vector machine method results: (A) oxygen permeability; (B) water vapour permeability; (C) initial degradation temperature; (D) maximum decomposition temperature.

Table 6 SVR results

Variable	Best C	Best ε	MSE (train)	R^2 (train)	MSE (test)	R^2 (test)
OP	100	0.01	1.037×10^{8}	2.327×10^{-2}	4.734×10^{7}	3.612×10^{-2}
WVP	100	0.01	9.931×10^{-5}	9.999×10^{-1}	1.068×10^{-1}	8.452×10^{-1}
T_{onset}	10	1	2.091×10^{2}	5.270×10^{-1}	5.556×10^{1}	6.804×10^{-1}
T_{10}	10	1	2.568×10^{2}	4.987×10^{-1}	6.447×10^{1}	7.114×10^{-1}
T_{max}	100	1	1.307×10^{2}	8.359×10^{-1}	2.801×10^{2}	1.375×10^{-2}

Table 7 ANNs results

Variable	R^2 test	R^2 train	MSE test	MAE test	Num layers	Num neurons	Epochs	Batch size
OP	9.302×10^{-1}	7.530×10^{-1}	4.000×10^{6}	1.633×10^{3}	6	100	50	16
WVP	9.968×10^{-1}	9.705×10^{-1}	5.432×10^{-3}	5.433×10^{-2}	2	110	50	16
T_{onset}	−5.083	−5.500	2.681×10^{3}	4.163×10^{1}	6	100	50	16
T_{10}	−4.963	-2.300×10^{1}	5.690×10^{3}	6.414×10^{1}	4	50	50	16
T_{max}	−3.734	−9.155	7.491×10^{3}	6.605×10^{1}	5	120	50	16

Finally, for the RF method, the hyperparameters studied were 'max_depth' = (none, 10, 20, 30), 'min_samples_leaf' = (1, 2, 3, 4), 'min_samples_split' = (2, 5, 10), and 'n_estimators' = (50, 100, 200). The results of the RF method are shown in Table 9.

Comparing the results of RF with DT, a significant improvement in the prediction of the variables is observed, favored by the inclusion of the number of trees in the forest, 'n_estimators'. Regarding the barrier properties, OP shows moderate overfitting given the difference between the training and validation R^2 values, although the MSA value is similar to other methods studied. WVP achieves better overall results than OP, both in accuracy and R^2. The dispersion of the predicted data is not large, as can be seen (see Fig. 9), so it could be an

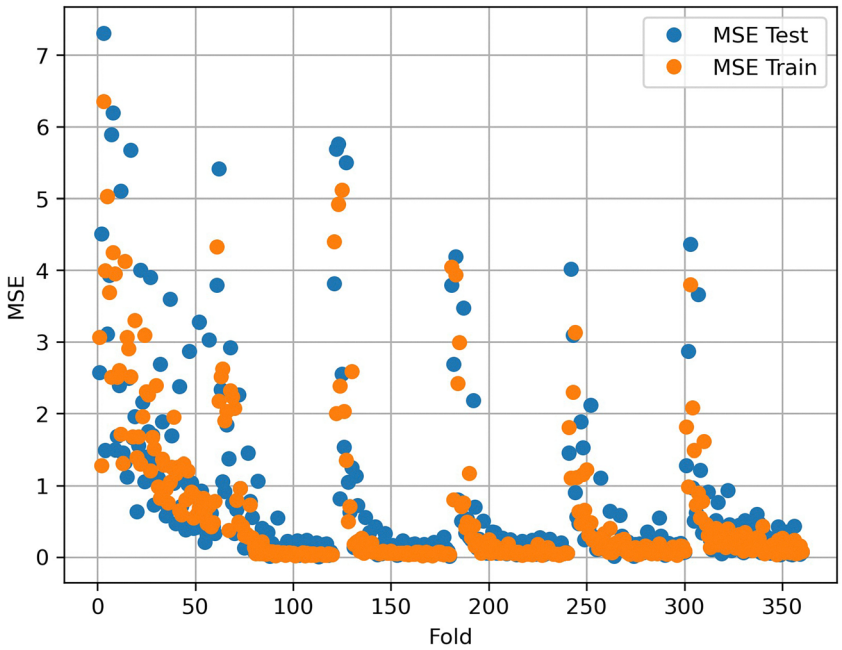

Fig. 8 Comparison of mean squared error (MSE·10^{-3}) results for ANNs model applied to water vapour permeability values.

Table 8 Results obtained upon application of the deep tree model to the different properties

Variable	Best hyperparameters	R^2 (train)	R^2 (test)	MSE (test)	MAE (test)
OP	{'max_depth': 5, 'max_features': none, 'min_samples_leaf': 1, 'min_samples_split': 5}	-2.914×10^{-2}	-8.613×10^{-1}	9.142×10^{7}	9.019×10^{3}
WVP	{'max_depth': 10, 'max_features': none, 'min_samples_leaf': 1, 'min_samples_split': 2}	1.734×10^{-1}	7.106×10^{-2}	6.413×10^{-1}	7.714×10^{-1}
T_{onset}	{'max_depth': 10, 'max_features': none, 'min_samples_leaf': 1, 'min_samples_split': 2}	-2.843×10^{-1}	-2.606	6.269×10^{2}	1.571×10^{1}
T_{10}	{'max_depth': 10, 'max_features': 'sqrt', 'min_samples_leaf': 1, 'min_samples_split': 2}	-3.871×10^{-2}	-2.831	8.559×10^{2}	2.271×10^{1}
T_{max}	{'max_depth': 3, 'max_features': 'sqrt', 'min_samples_leaf': 1, 'min_samples_split': 2}	-3.623×10^{-1}	-2.308	9.394×10^{2}	2.174×10^{1}

Table 9 Results obtained upon application of the RF model to the different properties

Variable	Best hyperparameters	MSE (test)	R^2 (train)	R^2 (test)	MSA (test)
OP	{'max_depth': none, 'min_samples_leaf': 1, 'min_samples_split': 2, 'n_estimators': 50}	3.323×10^{7}	9.494×10^{-1}	3.234×10^{-1}	5.055×10^{3}
WVP	{'max_depth': none, 'min_samples_leaf': 1, 'min_samples_split': 2, 'n_estimators': 200}	4.418×10^{-1}	9.585×10^{-1}	3.600×10^{-1}	5.894×10^{-1}
T_{onset}	{'max_depth': none, 'min_samples_leaf': 1, 'min_samples_split': 2, 'n_estimators': 200}	2.796×10^{2}	9.293×10^{-1}	-6.084×10^{-1}	1.119×10^{1}
T_{10}	{'max_depth': none, 'min_samples_leaf': 2, 'min_samples_split': 5, 'n_estimators': 100}	3.186×10^{2}	7.509×10^{-1}	-4.264×10^{-1}	1.497×10^{1}
T_{max}	{'max_depth': none, 'min_samples_leaf': 2, 'min_samples_split': 2, 'n_estimators': 200}	2.503×10^{2}	7.466×10^{-1}	1.185×10^{-1}	1.370×10^{1}

acceptable prediction model. The other variables are shown in Fig. S.8–S11.

On the other hand, although the prediction of the thermal properties showed better performance in training, the validation results did not improve accordingly. The fits for T_{onset} and T_{10} present excellent results in training, but in the validation scenario they show negative performance due to poor model generalization, which may be due to overfitting. In the case of T_{max}, better performance is observed compared to T_{10} and T_{onset}, but with modest applicability.

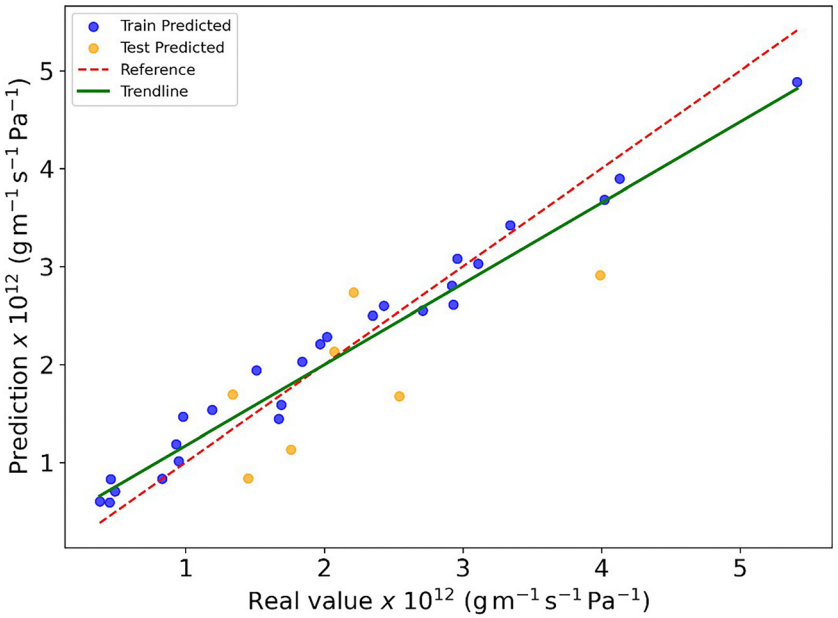

Fig. 9 Predicted values using random forest model *vs.* experimental values for water vapour permeability.

5. Conclusions

Hybrid bionanocomposites based on P3HB reinforced with sepiolite, CNTs and WS_2 have been successfully prepared by an easy, inexpensive and sustainable solution casting. SEM images revealed a very homogeneous nanofiller dispersion within the polyester matrix. FT-IR spectra suggest strong interactions among the nanofillers and with the matrix *via* hydrogen bonding. Thermogravimetric analysis revealed a very strong improvement in thermal stability upon nanofiller addition, particularly for the hybrids with high loading of CNTs and WS_2, with a maximum increase in T_{max} of about 125 °C, ascribed to a synergistic stabilization effect. Unprecedented drops in oxygen permeability and water vapour permeability have also been observed, the largest being 95 and 93%, respectively, for the nanocomposite with 2% Sep, 1% CNT and 2% WS_2. The accuracy of several machine learning models, including Lasso regression, polynomial regression, SVM, SVR, ANN, DT, and RF, on the prediction of thermal and barrier properties was assessed. The most effective models for barrier properties were ANNs and SVR, demonstrating high R^2 values and low MSE/MAE. For thermal properties, SVMs and SVR offered relatively better results, though with limited generalization. Given the limited size of the experimental dataset, the results should be interpreted with appropriate caution. The applied cross-validation-based methodology allows reliable comparison between models and identification of meaningful trends, rather than the development of universally generalizable predictive models. The good correlation between experimental and predicted values for barrier properties indicates that the models are reliable and consistent in this context, whereas thermal property predictions remain more challenging and model dependent.

Overall, the triple filler strategy applied herein is an original approach to develop hybrid nanocomposites with appropriate properties to be used in the food packing industry (*i.e.* as containers or disposable cutlery).

Author contributions

Ana M. Diez-Pascual: conceptualization, methodology, investigation, validation, formal analysis, writing – original draft, writing – review & editing, supervision. Jose A. Luceño-Sanchez: methodology, formal analysis, software; data curation, visualization, funding acquisition, writing – original draft, writing – review & editing.

Conflicts of interest

There are no conflicts to declare.

Data availability

All data used in this study are provided in the supplementary information (SI). Supplementary information: thermal and barrier properties of P3HB/SEP/MWCNT/WS_2 bionanocomposites; scoring results for Lasso regression; extended polynomial regression result for the prediction of barrier and thermal properties; schematic representation of DT, ANN and SVM models; comparative representation of polynomial regression models of three degrees for T_{max} T_{10} and OP; SVM confusion matrix for T_{10}; Predicted *vs.* experimental values using RF model for OP, T_{max} and T_{10}. See DOI: https://doi.org/10.1039/d5nj03812j.

Additional data will be available on request.

Acknowledgements

Dr JALS acknowledges the Juan de la Cierva Fellowship (JDC2022-048676-I), co-funded by the European Next Generation EU Fund and the Spanish Ministry of Universities, Innovation and Science.

References

1 A. M. Díez-Pascual and A. L. Díez-Vicente, ZnO-Reinforced Poly(3-hydroxybutyrate-*co*-3-hydroxyvalerate) Bionanocomposites with Antimicrobial Function for Food Packaging, *ACS Appl. Mater. Interfaces*, 2014, **6**, 9822–9834.

2 J. Meimoun, A. Favrelle-Huret, J. D. Winter and P. Zinck, Poly(L-lactide) Epimerization and Chain Scission in the Presence of Organic Bases, *Macromol*, 2022, **2**, 236–246.

3 A. M. Díez-Pascual and A. L. Díez-Vicente, Poly(3-hydroxybutyrate)/ZnO Bionanocomposites with Improved Mechanical, Barrier and Antibacterial Properties, *Int. J. Mol. Sci.*, 2014, **15**, 10950–10973.

4 L. García-Quiles, Á. F. Cuello and P. Castell, Sustainable Materials with Enhanced Mechanical Properties Based on Industrial Polyhydroxyalkanoates Reinforced with Organomodified Sepiolite and Montmorillonite, *Polymers*, 2019, **11**, 696.

5 P. Cataldi, P. Steiner, T. Raine, K. Lin, C. Kocabas, R. J. Young, M. Bissett, I. A. Kinloch and D. G. Papageorgiou, Multifunctional Biocomposites Based on Polyhydroxyalkanoate and Graphene/Carbon Nanofiber Hybrids for Electrical and Thermal Applications, *ACS Appl. Polym. Mater.*, 2020, **2**, 3525–3534.

6 A. M. Díez-Pascual, B. Ashrafi, M. Naffakh, J. M. González-Domínguez, A. Johnston, B. Simard, M. T. Martínez and M. A. Gómez-Fatou, Influence of carbon nanotubes on the thermal, electrical and mechanical properties of poly(ether ether ketone)/glass fiber laminates, *Carbon*, 2011, **49**, 2817–2833.

7 S. Uppugalla, R. Pothu and R. Boddula, Nitrogen and sulfur co-doped activated carbon nanosheets for high-performance coin cell supercapacitor device with outstanding cycle stability, *Emergent Mater.*, 2023, **6**, 1167–1176.

8 A. M. Díez-Pascual and D. Gascón, Carbon Nanotube Buckypaper Reinforced Acrylonitrile–Butadiene–Styrene Composites for Electronic Applications, *ACS Appl. Mater. Interfaces*, 2013, **5**, 12107–12119.

9 A. M. Díez-Pascual, Chemical Functionalization of Carbon Nanotubes with Polymers: A Brief Overview, *Macromol*, 2021, **1**, 64–83.

10 A. M. Díez-Pascual and A. Rahdar, Composites of Vegetable Oil-Based Polymers and Carbon Nanomaterials, *Macromol*, 2021, **1**, 276–292.

11 K. Aschberger, Review of carbon nanotubes toxicity and exposure—Appraisal of human health risk assessment based on open literature, *Crit. Rev. Toxicol.*, 2010, **40**, 759–790.

12 A. Bianco, K. Kostarelos and M. Prato, Making carbon nanotubes biocompatible and biodegradable, *Chem. Commun.*, 2011, **47**, 10182–10188.

13 G. Biddeci, G. Spinelli, P. Colomba and F. Di Blasi, Halloysite Nanotubes and Sepiolite for Health Applications, *Int. J. Mol. Sci.*, 2023, **24**, 4801.

14 E. Ruiz-Hitzky, P. Aranda, M. Darder and F. M. Fernandes, Fibrous Clay Mineral–Polymer Nanocomposites, in *Developments in Clay Science*, ed. F. Bergaya and G. Lagaly, Elsevier Ltd, 2013, ch. 13.3, vol. 5, pp. 721–741.

15 M. Naffakh, A. M. Díez-Pascual and M. A. Gómez-Fatou, New hybrid nanocomposites containing carbon nanotubes, inorganic fullerene-like WS2 nanoparticles and poly(ether ether ketone) (PEEK), *J. Mater. Chem.*, 2011, **21**, 7425–7433.

16 W. Z. Teo, E. L. K. Chng, Z. Sofer and M. Pumera, Cytotoxicity of Exfoliated Transition-Metal Dichalcogenides (MoS2, WS2, and WSe2) is Lower Than That of Graphene and its Analogues, *Chem. – Eur. J.*, 2014, **20**, 9627–9632.

17 M. Naffakh, A. M. Díez-Pascual, C. Marco, G. J. Ellis and M. A. Gómez-Fatou, Opportunities and challenges in the use of inorganic fullerene-like nanoparticles to produce advanced polymer nanocomposites, *Prog. Polym. Sci.*, 2013, **38**, 1163–1231.

18 D. Makwakwa, M. P. Motloung, V. Ojijo, J. Bandyopadhyay and S. S. Ray, Influencing the Shape Recovery and Thermomechanical Properties of 3DP PLA Using Smart Textile and Boehmite Alumina and Thermochromic Dye Modifiers, *Macromol*, 2022, **2**, 485–499.

19 D. M. Videira Quintela, F. Guillén Carretero, O. Martín Cádiz, L. Cumbal and G. Montalvo García, Antibacterial and antioxidant triple-side filler composed of fumed silica, iron, and tea polyphenols for active food packaging, *Food Control*, 2022, **138**, 109036.

20 D. Parajuli, S. Uppugalla, N. Murali, A. Ramakrishna and B. Suryanarayana, Synthesis and characterization MXene-Ferrite nanocomposites and its application for dying and shielding, *Inorg. Chem. Commun.*, 2023, **148**, 110319.

21 A. Saha and S. Kumar, Effects of graphene nanoparticles with organic wood particles: A synergistic effect on the structural, physical, thermal, and mechanical behavior of hybrid composites, *Polym. Adv. Tehcnol.*, 2022, **33**, 3201–3215.

22 M. S. Kumar, S. Kumar, K. Gouda and S. Bhowmik, Influence of filler hybridization on thermomechanical properties of hemp/silver epoxy composite, *Polym. Polym. Compos.*, 2021, **29**, 1551–1562.

23 M. I. Jordan, Artificial Intelligence-The Revolution Hasn't Happened Yet, *Harvard Data Sci. Rev.*, 2019, **1**, 1.

24 Y. Wang, M. Zhang, A. Lin, A. Iyer, A. S. Prasad, X. Li, Y. Zhang, L. S. Schadler, W. Chen and L. C. Brinson, Mining structure-property relationships in polymer nanocomposites using data driven finite element analysis and multi-task convolutional neural networks, *Mol. Sys. Design Eng.*, 2020, **5**, 962–975.

25 Z. Shen, H. Liu, Y. Shen, J. Hu, L. Chen and C. Nan, Machine learning in energy storage materials, *Interdiscip. Mater.*, 2022, **1**, 175–195.

26 E. Champa-Bujaico, P. García-Díaz and A. M. Díez-Pascual, Machine Learning for Property Prediction and Optimization of Polymeric Nanocomposites: A State-of-the-Art, *Int. J. Mol. Sci.*, 2022, **23**, 10712.

27 M. Özkan, A. Karakoç, M. Borghei, J. Wiklund, O. J. Rojas and J. Paltakari, Machine Learning assisted design of tailor-made nanocellulose films: A combination of experimental and computational studies, *Polym. Compos.*, 2019, **40**, 4013–4022.
28 V. Kumar Mahakur, S. Bhowmik and P. Kumar Patowari, Tribo-informatics evaluation of dry sliding friction of silanized jute filler reinforced epoxy composites using machine learning techniques, *Tribol. Int.*, 2023, **183**, 108388.
29 S. K. Sahu and P. S. R. Sreekanth, Artificial Neural Network for Prediction of Mechanical Properties of HDPE Based Nanodiamond Nanocomposite, *Polymer*, 2022, **46**, 614–620.
30 L. Natrayan, A. Bhaskar, P. P. Patil, S. Kaliappan, M. Dineshkumar and E. S. Esakkiraj, Optimization of Filler Content and Size on Mechanical Performance of Graphene/Hemp/Epoxy-Based Hybrid Composites using Taguchi with ANN Technique, *J. Nanomater.*, 2023, **5**, 1–15.
31 A. Khan, M. H. Shamsi and T. Choi, Correlating dynamical mechanical properties with temperature and clay composition of polymer-clay nanocomposites, *Comput. Mater. Sci.*, 2009, **45**, 257–265.
32 K. T. Butler, D. W. Davies, H. Cartwright, O. Isayev and A. Walsh, Machine learning for molecular and materials science, *Nature*, 2018, **559**, 547–555.
33 B. de Ville, Decision trees, *Wiley Interdiscip. Rev.: Comput. Stat.*, 2013, **5**, 448–455.
34 W. Loh, Classification and regression trees, *Wiley Interdiscip. Rev.:Data Min. Knowl. Dis.*, 2011, **1**, 14–23.
35 R. G. Mantovani, T. Horváth, A. L. D. Rossi, R. Cerri, S. Barbon Junior, J. Vanschoren and A. C. P. L. de Carvalho, Better Tress: An empirical study on hyperparameter tuning of decision trees, *Data Min. Knowl. Dis.*, 2024, **38**, 1364–1416.
36 P. J. Drew and J. R. T. Monson, Artificial neural networks, *Surgery*, 2000, **127**, 3–11.
37 J. Zou, Y. Han and S. So, Overview of Artificial Neural Networks, *Methods Mol. Biol.*, 2008, **458**, 14–22.
38 F. Rosenblatt, Basis definitions and concepts, *Principles of neurodynamics; perceptrons and the theory of brain mechanisms*, Spartan Books, Washington (State), 1962, pp. 79–92.
39 A. K. Jain, M. Jianchang and K. M. Mohiuddin, Artificial neural networks: a tutorial, *Computer*, 1996, **29**, 31–44.
40 S. B. Lo, H. Chan, J. Lin, H. Li, M. T. Freedman and S. K. Mun, Artificial convolution neural network for medical image pattern recognition, *Neural Networks*, 1995, **8**, 1201–1214.
41 T. Hristeva, Application of graphic processing units in deep learning algorithms, *AIP Conf. Proc.* 2449 (2022) 1.
42 C. Cortes and V. Vapnik, Support-vector networks, *Mach. Learn.*, 1995, **20**, 273–297.
43 N. Cristianini and J. Shawe-Taylor, Suppoert Vector Machines, *An Introduction to Support Vector Machines and Other Kernel-Based Learning Methods*, Cambridge University Press, Cambridge, 2000, pp. 93–122.
44 N. S. Raghavendra and P. C. Deka, Support vector machine applications in the field of hydrology: A review, *Appl. Soft Comput.*, 2014, **19**, 372–386.
45 C.-W. Hsu and C.-J. Lin, A comparison of methods for multiclass support vector machines, *IEEE Trans. Neural Networks*, 2002, **13**, 415–425.
46 H. Qian, E. S. Greenhalgh, M. S. P. Shaffer and A. Bismarck, Carbon Nanotube-Based Hierarchical Composites: A Review, *J. Mater. Chem.*, 2010, **20**, 4751–4762.
47 A. Kumar, A. Saha and S. Kumar, Structural analysis of sol-gel derived TiO2 nanoparticles: a critical impact of TiO2 nanoparticles on thermo-mechanical mechanism of glass fiber polymer composites, *J. Polym. Res.*, 2021, **28**, 441.
48 M. Zakaulla, Y. Pasha and S. K. Siddalingappa, Prediction of mechanical properties for polyetheretherketone composite reinforced with graphene and titanium powder using artificial neural network, *Mater. Today: Proc.*, 2022, **49**, 1268–1274.
49 Y. Sarıkaya, M. Önal and A. D. Pekdemir, Thermal degradation kinetics of sepiolite, *Clay Miner.*, 2020, **55**, 96–100.
50 A. M. Diez-Pascual, G. Martinez, J. Gonzalez-Dominguez, A. Anson, M. T. Martinez and M. Gomez, Grafting of a hydroxylated poly(ether ether ketone) to the surface of single-walled carbon nanotubes, *J. Mater. Chem.*, 2010, **2**, 8285–8296.
51 A. M. Diez-Pascual, J. W. Guan, B. Simard and M. A. Gómez-Fatou, Poly(phenylene sulphide) and poly (ether ether ketone) composites reinforced with single-walled carbon nanotube buckypaper: II – Mechanical properties, electrical and thermal conductivity, *Composites, Part A*, 2012, **43**, 1007–1015.
52 H. Ma, L. Tong, Z. Xu and Z. Fang, Synergistic effect of carbon nanotube and clay for improving the flame retardancy of ABS resin, *Nanotechnology*, 2007, **18**, 375602.
53 Z. Zhang, Y. Xie, Y. Ouyang and Y. Chen, A systematic investigation of thermal conductivities of transition metal dichalcogenides, *Int. J. Heat Mass Transfer*, 2017, **108**, 417–422.
54 F. Özdemir, A. Çot and H. Alma, Effect of sepiolite mineral on thermal properties and thermal conductivity of wood plastic composite materials, *Turk. J. Agric. For.*, 2018, **19**, 205–209.
55 K. Jlassi, M. M. Chehimi and S. Thomas, Sepiolite-Reinforced Polymer Nanocomposites, in *Clay-Polymer Nanocomposites*, ed. K. Jlassi, M. M. Chehimi and S. Thomas, Elsevier, 2017, pp. 47–48.
56 J.-Y. Chen, X.-W. Zhang, T.-Y. Wu and H.-M. Ye, Co-Crystallization between Aliphatic Polyesters through Co-Inclusion Complexation with Small Molecule, *Molecules*, 2023, **28**, 4091.
57 Y.-Y. Song, H.-M. Ye, X.-Y. Meng, Q. Zhou and G.-W. Lu, Novel polymorphism behavior of poly(butylene adipate) in its nanocomposites with carbon nanofibers, *RSC Adv.*, 2015, **5**, 12384–12391.
58 C. J. Serna and G. E. Vanscoyoc, Infrared Study of Sepiolite and Palygorskite Surfaces, *Dev. Sedimentol.*, 1979, **27**, 197–206.
59 V. Siracusa, Food Packaging Permeability Behaviour: A Report, *Int. J. Polym. Sci.*, 2012, **4**, 1687–9422.
60 D. S. Lee, K. L. Yam and L. Piergiovanni, *Food Packaging Science and Technology*, CRC Press, Taylor & Francis Group, 2008.

61 A. S. Sethulekshmi, J. S. Jayan, A. Saritha and J. Kuruvilla, Insights into the reinforcibility and multifarious role of WS2 in polymer matrix, *J. Alloys Compd.*, 2021, **876**, 160107.
62 M. D. Sanchez-Garcia and J. M. Langaron, Novel clay-based nanobiocomposites of biopolyesters with synergistic barrier to UV light, gas, and vapour, *J. Appl. Polym. Sci.*, 2010, **118**, 188–199.
63 E. L. Papadopoulou, P. Basnett, U. C. Paul, S. Marras, L. Ceseracciu, I. Roy and A. Athanassiou, Green Composites of Poly(3-hydroxybutyrate) Containing Graphene Nanoplatelets with Desirable Electrical Conductivity and Oxygen Barrier Properties, *ACS Omega*, 2019, **4**, 19746–19755.
64 T. D. Hapuarachchi and P. Ton, Multiwalled carbon nanotubes and sepiolite nanoclays as flame retardants for polylactide and its natural fibre reinforced composites, *Composites, Part A*, 2010, **41**, 954–963.
65 D. Li, H. Liu, X. He, Y. Yao, H. Liu, J. Chen, B. Deng and X. Lan, Sepiolite-Supported Manganese Oxide as an Efficient Catalyst for Formaldehyde Oxidation: Performance and Mechanism, *Molecules*, 2024, **29**, 2826.

